Electronic Supplementary Information for

Bandgap Lowering in Mixed Alloys of $Cs_2Ag(Sb_xBi_{1-x})Br_6$ Double Perovskite Thin Films

Zewei Li,[,1,†] Seán R. Kavanagh,[*,2,3,4,†] Mari Napari,[5] Robert G. Palgrave,[2] Mojtaba Abdi-Jalebi,[6] Zahra Andaji-Garmaroudi,[1] Daniel W. Davies,[2,4] Mikko Laitinen,[7] Jaakko Julin,[7] Mark A. Isaacs,[2,8] Richard H. Friend,[1] David O. Scanlon,[2,4,9] Aron Walsh,[3,10] and Robert L. Z. Hoye[*,3]*

[1] Cavendish Laboratory, Department of Physics, University of Cambridge, JJ Thomson Avenue, Cambridge CB3 0HE, UK

[2] Department of Chemistry, University College London, 20 Gordon Street, London WC1H 0AJ, UK

[3] Department of Materials, Imperial College London, Exhibition Road, London SW7 2AZ, UK

[4] Thomas Young Centre, University College London, Gower Street, London WC1E 6BT, UK

[5] Zepler Institute for Photonics and Nanoelectronics, University of Southampton, University Road, Southampton SO17 1BJ, UK

[6] Institute for Materials Discovery, University College London, Torrington Place, London WC1E 7JE, UK

[7] Department of Physics, University of Jyväskylä, P.O. Box 35, 40014 University of Jyväskylä, Finland

[8] HarwellXPS, Research Complex at Harwell, Harwell Science and Innovation Campus, Didcot, Oxfordshire OX11 0DE, UK

[9] Diamond Light Source Ltd., Diamond House, Harwell Science and Innovation Campus, Didcot, Oxfordshire OX11 0DE, UK

[10] Department of Materials Science and Engineering, Yonsei University, Seoul 120-749, South Korea

† These authors contributed equally

∗Correspondence to:

zl362@cam.ac.uk (Z.L.)

sean.kavanagh.19@ucl.ac.uk (S.R.K.)

r.hoye@imperial.ac.uk (R.L.Z.H.)

EXPERIMENTAL

Film deposition

1.5 mmol CsBr (99.9%, Sigma Aldrich), 0.75 mmol AgBr (99.998%, Alfa Aesar), and 0.75 mmol $SbBr_3$ (99.99%, Sigma Aldrich) were dissolved in 1.5 mL anhydrous dimethyl sulfoxide DMSO (99.9%, Sigma Aldrich) and mixed at 700 rpm at room temperature (RT) inside a N_2 glovebox for an hour. Another 1.5 mmol CsBr (99.9%, Sigma Aldrich), 0.75 mmol AgBr (99.998%, Alfa Aesar), and 0.75 mmol $BiBr_3$ (99.998%, Sigma Aldrich) were dissolved in 1.5 mL anhydrous DMSO (99.9%, Sigma Aldrich) and mixed at 700 rpm at RT inside a N_2 glovebox for an hour. Both solutions were then filtered by 0.2 μm PTFE membranes (Sigma Aldrich). 0.45 mL $Cs_2AgSbBr_6$ solution was mixed with 0.05 mL $Cs_2AgBiBr_6$ solution to form the 90% Sb Sb-Bi solution. 0.35 mL $Cs_2AgSbBr_6$ solution was mixed with 0.15 mL $Cs_2AgBiBr_6$ solution to form the 70% Sb Sb-Bi solution. 0.25 mL $Cs_2AgSbBr_6$ solution was mixed with 0.25 mL $Cs_2AgBiBr_6$ solution to form the 50% Sb Sb-Bi solution. 0.1 mL $Cs_2AgSbBr_6$ solution was mixed with 0.4 mL $Cs_2AgBiBr_6$ solution to form the 20% Sb Sb-Bi solution. 12 mm × 12 mm glass substrates were cleaned by ultrasonication in acetone and isopropanol for 15 min sequentially, followed by 10 min O_2 plasma cleaning at 300 W (forward power) in a radio frequency (RF) plasma system. The substrates were subsequently taken into a N_2 glovebox and preheated to 75 °C. Precursor solutions containing Sb were kept at room temperature. Precursor solution with pure $Cs_2AgBiBr_6$ was preheated to 75 °C. To deposit the films, the substrate was placed onto a vacuum-free chuck, and 60 μL solution was immediately dropped onto the substrate, before spinning at 4000 rpm for 45 s. Substrates containing Sb were annealed at 135 °C for 5 min. Substrates with pure $Cs_2AgBiBr_6$ were annealed at 250 °C for 5 min. The spin coating and annealing process were undertaken in the N_2 glovebox.

Computations

All calculations were performed using Density Functional Theory (DFT) within periodic boundary conditions through the Vienna Ab Initio Simulation Package (VASP).[1–4] The PBEsol DFT functional was used for geometry optimizations and calculations of static dielectric constants,[5] while the hybrid functional HSE06 was implemented for band structure, band offset and optical calculations.[6] To fully account for relativistic effects, spin-orbit interactions were included (HSE06+SOC) in all electronic and optical calculations. HSE06 is a range-separated, screened hybrid-DFT functional which incorporates 25% exact Hartree-Fock exchange for short-range interactions, using a screening parameter $\omega = 0.11$ bohr^{-1}, with the remaining exchange-correlation effects treated by the Generalized Gradient Approximation (GGA) DFT functional PBE.[7] Scalar-relativistic pseudopotentials were employed, and the projector-augmented wave (PAW) method was used to describe the interaction between core and valence electrons.[8] The ionic dielectric response was calculated under Density Functional Perturbation Theory (DFPT),[9] while the optical response was calculated using the method of Furthmüller et al. to obtain the high-frequency real and imaginary dielectric functions.[9] A convergence criterion of 1 meV/Å was imposed on the forces on each atom during structural optimization. Bulk electronic structure calculations were carried out using a $5 \times 5 \times 5$ Monkhorst-Pack k-point mesh and a well-converged 550 eV plane-wave cutoff, while a tighter k-mesh of $9 \times 9 \times 9$ was used for the optical calculations. Charge carrier effective masses were obtained from non-parabolic fitting of the electronic band edges using the *effmass* package,[10] while electronic band structure diagrams were generated using the *sumo* package.[11] For each calculation, convergence with respect to k-point density and plane-wave energy cutoff was confirmed for the property of interest.

Band alignment:

In order to calculate the relative alignment of the electron bands, the electrostatic potential offset between the two materials, ΔV, was required. This was determined using the method of Butler *et al.*,[12] with calculated values for ΔV verified by comparison with relative core-level energy shifts. A 160-atom heterojunction supercell of length 89 Å, consisting of eight primitive unit cells each of $Cs_2AgSbBr_6$ and $Cs_2AgBiBr_6$, was generated using the average lattice parameter of the two structures, with no interfacial atomic relaxation permitted. Electronic relaxation of this interface with hybrid-DFT yielded a value for the electrostatic potential offset ΔV between the two bulk materials, from which the alignment of electronic states in the two materials could be determined, according to equations S1 and S2. In order to account for the opposing changes in electrostatic potentials of the materials upon formation of the average-lattice-constant supercell, the absolute volume deformation potentials (ADVPs) $a_v^i = \frac{dV^i}{d(\ln(v))}$ were calculated for both materials using the method of Wei et al.[13,14] Within this method, an angular average is performed over the uniaxial deformation potentials $a_r^i = \frac{dV^i}{d(\ln(r))}$, determined via a series of strained-homojunction supercell calculations, to yield a value for a_v^i.

$$\text{Valence Band Offset (VBO)} = \epsilon^A{}_{VBM} - \epsilon^B{}_{VBM} + \Delta V + a_v^A d(\ln(v_A)) + a_v^B d(\ln(v_B)) \quad \text{S1}$$

$$\text{Conduction Band Offset (CBO)} = \epsilon^A{}_{CBM} - \epsilon^B{}_{CBM} + \Delta V + a_v^A d(\ln(v_A)) + a_v^B d(\ln(v_B)) \quad \text{S2}$$

$$\text{CBO} = \text{VBO} + E_{g,A} - E_{g,B} + a_v^A d(\ln V_A) + a_v^B d(\ln V_B) \quad \text{S3}$$

In the above equations, $\epsilon^i{}_{VBM}$ and $\epsilon^i{}_{CBM}$ are the eigenvalues (referenced to the average electrostatic potential) of the VBM and CBM for the ideal bulk material i, while $d(\ln(v_i)) = \frac{\Delta v_i}{v_i}$ is the relative volume change between the equilibrium structure of i and the average-lattice-constant unit in the supercell. $E_{g,i}$ is the fundamental band gap of material i. Convergence of the potential offset ΔV with respect to supercell size was verified by repeating the calculation

with 80-atom (45 Å) and 120-atom cells (68 Å). While hybrid DFT (HSE06) was used in these supercell alignment calculations, in order to ensure accuracy and consistency, it is noted that both LDA and GGA standard DFT gave matching results in each case to within 0.02 eV (for the electrostatic potential offset ΔV).

Alloy Band Structures:

Although an in-depth, fully-consistent theoretical analysis of the structural, thermodynamic and electronic properties of the mixed Sb-Bi double perovskite alloys was beyond the scope of this work, the thermodynamic and electronic properties of a selection of probable alloy structures were investigated.

Using 80-atom supercells (2 × 2 × 2 cubic expansion of the 10-atom unit cell), corresponding to $Cs_2AgSb_{0.125}Bi_{0.875}Br_6$ (12.5 at% Sb concentration), $Cs_2AgSb_{0.5}Bi_{0.5}Br_6$ (50/50 at% Sb/Bi) - in two possible uniform, homogeneous arrangements, and $Cs_2AgSb_{0.75}Bi_{0.25}Br_6$ (75% at% Sb conc.)(Figure S13), the free energies of mixing and electronic band structures for these representative alloy materials were determined, with full inclusion of spin-orbit coupling effects.

The symmetry-weighted unfolded bandstructures for these materials are shown in Figure S14, with the corresponding fundamental bandgaps provided in Table S3. In each case, the alloy materials exhibit the experimentally-observed bandgap lowering, relative to the pure materials.

The corresponding electronic density of states for each case is shown in Figure S15, demonstrating the predicted Bi *p* – Br *p* dominated CBM (with some Sb *p* character) and Sb *s* – Ag *d* – Br *p* dominated VBM (with some Bi *s* character), in agreement with the prediction

that non-linear orbital mixing at the band edges is the source of the experimentally-observed bandgap lowering. Moreover, the minimum bandgap is observed at high concentrations of antimony (75 at% Sb), in good agreement with our experimental observations (Figure 3d).

Predicted XPS plots for the alloy and pure material compositions were generated from the calculated electronic density of states using the *galore* package.[15]

The free energy of mixing (ΔG_{mix}) was calculated using the following relations:

$$\Delta G_{Mix} = \Delta H_{Mix} - T\Delta S_{Mix\,(Configurational)} \quad \text{S4}$$

$$\Delta S_{Mix\,(Configurational)} = -N k_b (x_A ln x_A + x_B ln x_B) \quad \text{S5}$$

The results of the calculations of the free energy of mixing are shown in Figure S17. In agreement with experimental observations,[16] concentrations of up to ~60 at% Sb are predicted to be thermodynamically stable with respect to phase separation. However, it should be noted that a comprehensive theoretical investigation of the alloy stability would require explicit calculations for a range of possible structural arrangements (i.e. clustered, disordered, quasi-random etc.) at each alloy concentration, which could correspond to lower free energies of mixing, but are beyond the scope of this work.

Characterization

Diffraction measurement:

1D X-ray Diffraction (XRD) was carried out on films in air at room temperature with a B3 Bruker D8 DAVINCI instrument employing Cu K_α radiation.

2D thin film XRD was measured with a Bruker D8 Davinci diffractometer in reflection geometry. The incident X-ray beam was microfocused and columnated to a 2 mm^2 spot on the sample surface. A 2D area detector was used and the sample was held on an Eulerian cradle. Diffraction patterns were obtained over two frames of the 2D detector. Data analysis was carried out using Bruker Multex 3 software.

Composition measurement:

Rutherford Backscattering Spectrometry (RBS) data were measured with 5.115 MeV $^7Li^{2+}$ ion beam. The incident beam with a spot size of ca. 1.5 mm × 3 mm was parallel to surface normal (sample tilt 0°) and the backscattering angle was 165°. The beam fluence was normalized with the backscattering counts from the Au-coated chopper and sample substrate. The acquired RBS spectra were analyzed using SimNRA simulation software to determine the elemental composition of the films.[17] The uncertainty of the elemental fractions is in the order of 1%, and is based on the estimated statistical error of the backscattering yield (proportional to $1/\sqrt{N}$), the uncertainty of the simulation parameters for the peak fitting, as well as the uncertainties arising from the detector setup.

Morphology measurement:

Scanning Electron Microscopy (SEM) images were obtained with LEO 1530 VP instrument. Before taking SEM images, films were sputtered with Au/Pd source for 7 s at 65 mA using the Emitech sputter coater.

Absorption measurement:

UV–Visible Spectrophotometry measurements were performed using a PerkinElmer Lambda 750 spectrometer inside an integrating sphere. The reflectance and transmittance of the $Cs_2AgBiBr_6$ thin film on glass were separately measured. The instrument was calibrated to 0% and 100% reflectance/transmittance prior to measuring the sample. The measurements were taken from 900 to 300 nm wavelength with an interval of 5 nm. The absorption coefficient was calculated using Eq. S6 shown below

$$\alpha = \frac{\ln\left(\frac{1-R}{T}\right)}{d} \qquad \text{S6}$$

Where α is absorption coefficient, T is transmittance, R is reflectance and d is the measured thickness of the thin film, approx. 200 nm (from Dektak profilometry).

Photothermal Deflection Spectroscopy (PDS) is an ultrasensitive absorption measurement technique that detects heating of the sample due to the nonradiative relaxation of absorbed light and is insensitive to reflection and scattering. PDS enables the detection of absorbance signals with 5-6 orders of magnitude weaker than the band edge absorption. For the measurements, a monochromatic Pump light beam is shined on the sample (film on quartz substrate), which on absorption produces a thermal gradient near the sample surface via non-radiative relaxation induced heating. This results in a refractive index gradient in the area surrounding the sample surface. This refractive index gradient is further enhanced by immersing the sample in an inert liquid FC-72 Fluorinert® (3M Company) which has a high refractive index change per unit

change in temperature. A fixed wavelength CW laser probe beam is passed through this refractive index gradient producing a deflection proportional to the absorbed light at that particular wavelength, which is detected by a photodiode and lock-in amplifier combination. Scanning through different wavelengths gives us the complete absorption spectra. Because this technique makes use of the non-radiative relaxation processes in the sample, it is immune to optical effects like interference and scattering.

Band position measurement:

Photoemission spectroscopy:

XPS data was acquired using a Kratos Axis SUPRA using monochromated Al K_α (1486.69 eV) X-rays at 12 mA emission and 15 kV HT (180W) and a spot size/analysis area of 700 × 300 μm^2. The instrument was calibrated to gold metal Au 4f core level (83.95 eV) and dispersion adjusted give a binding energy (BE) of 932.6 eV for the Cu $2p_{3/2}$ line of metallic copper. Ag $3d_{5/2}$ line FWHM at 10 eV pass energy was 0.544 eV. Source resolution for monochromatic Al K_α X-rays is ~0.3 eV. The instrumental resolution was determined to be 0.29 eV at 10 eV pass energy using the Fermi edge of the valence band for metallic silver. Resolution with charge compensation system on <1.33 eV FWHM on PTFE. High resolution spectra were obtained using a pass energy of 20 eV, step size of 0.1 eV and sweep time of 60 s, resulting in a line width of 0.696 eV for Au $4f_{7/2}$. Survey spectra were obtained using a pass energy of 160 eV. Charge neutralization was achieved using an electron flood gun with filament current = 0.38 A, charge balance = 2 V, filament bias = 4.2 V. Successful neutralization was adjudged by analyzing the C 1s region wherein a sharp peak with no lower BE structure was obtained. The spectra were charge corrected to the main line of the carbon 1s spectrum (adventitious carbon) set to 284.8 eV. All data was recorded at a base pressure of below 9 x 10^{-9} Torr and a room temperature of 294 K. Data was analysed using CasaXPS v2.3.19PR1.0. Peaks were fit with a Shirley background prior to component analysis. UPS

measurements were recorded using He(I) (21.22 eV) at an emission of 35 mA. All UPS spectra were recorded at a pass energy of 5eV. UPS spectra were aligned to the recorded XPS valence bands through peak fitting of the Cs $5p_{3/2}$ species using an LA(1,3,230) lineshape for both sets of spectra.

The work function was determined by linear fitting of the secondary-electron cut-off of the ultraviolet photoemission spectra. The valence band to Fermi level offset (E_F – VB) was determined by least-squares fitting of the leading-edge of the X-ray photoemission spectroscopy (XPS) valence band spectra with the calculated XPS plots. The ionization potential was determined from the work function and E_F – VB measurements. The electron affinity was calculated by subtracting the bandgap measured by PDS from the ionization potential.

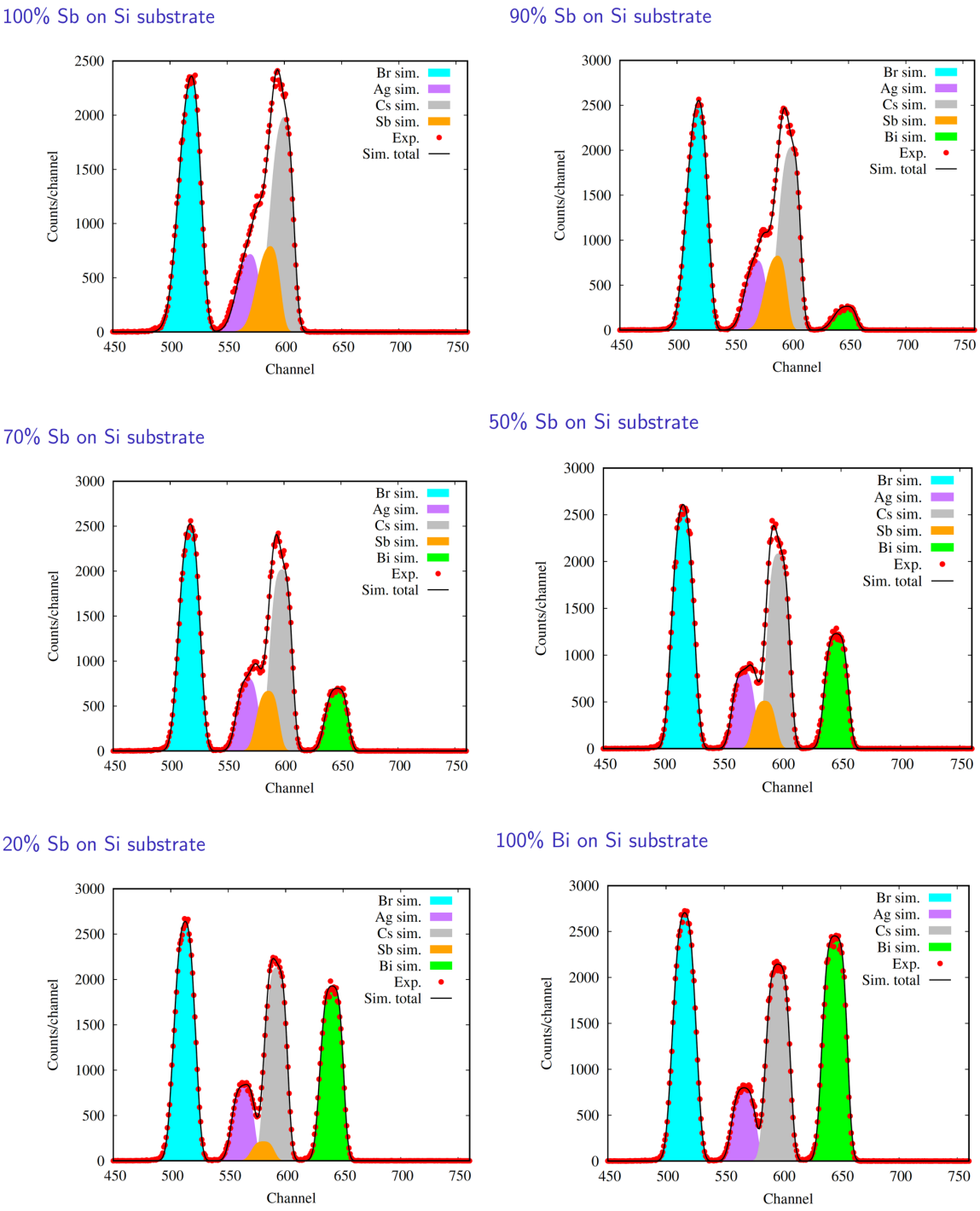

Figure S1. Rutherford Backscattering Spectrometry measurements for $Cs_2Ag(Sb_xBi_{1-x})Br_6$ films deposited on silicon substrates, along with the fits used to determine the composition. The "X% Sb/Bi on Si substrate" are the nominal values of the precursor solution used to deposit the films.

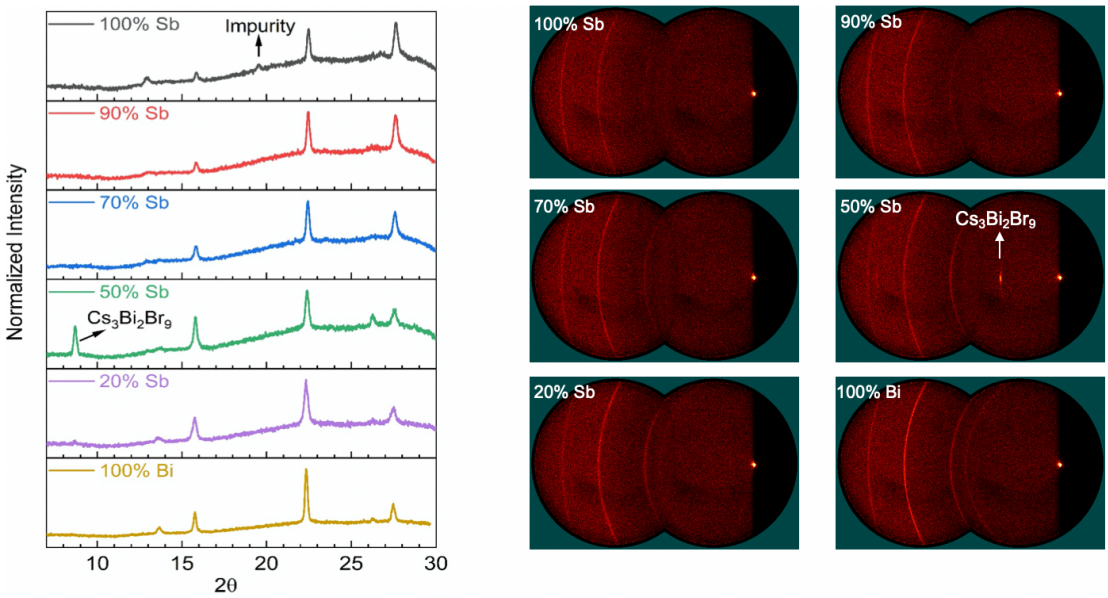

Figure S2. 2D XRD of $Cs_2Ag(Sb_xBi_{1-x})Br_6$ thin films, characterized on glass. The 8.9° peak of $Cs_3Bi_2Br_9$ at the 2D scan matches well with the peak in 1D linescan.

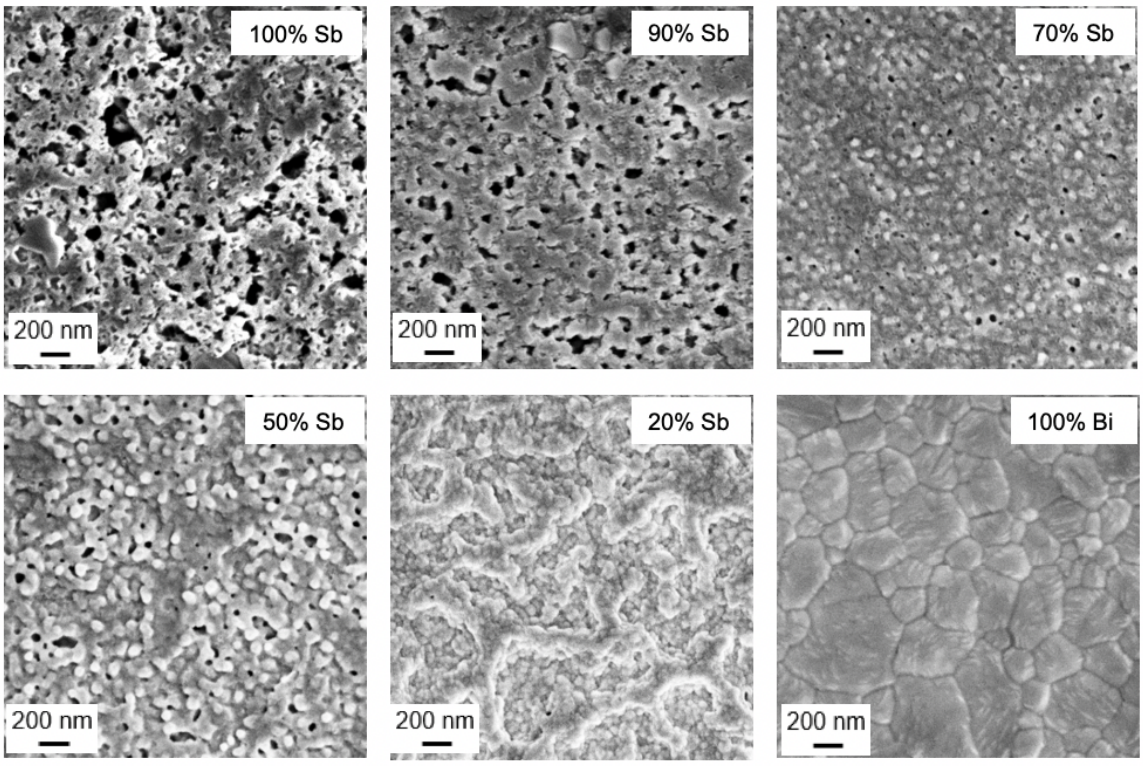

Figure S3. SEM of $Cs_2Ag(Sb_xBi_{1-x})Br_6$ thin films, characterized on glass. Only the $Cs_2AgBiBr_6$ exhibits a large grain size and good morphology.

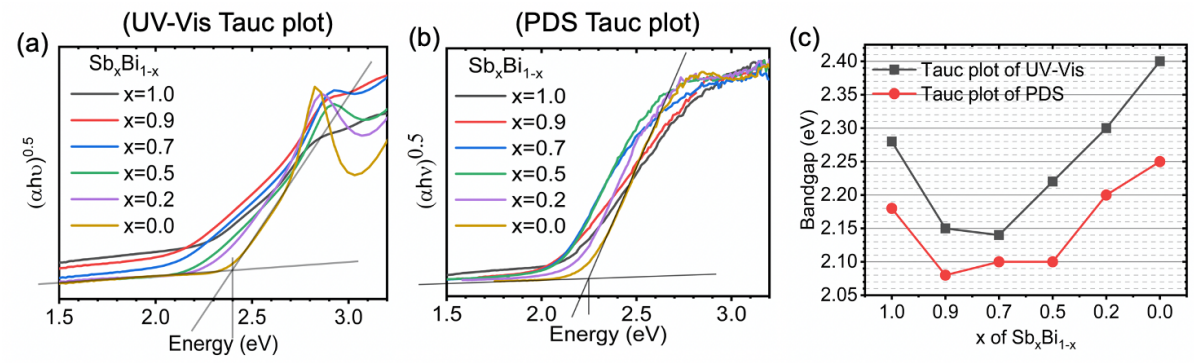

Figure S4. (a) Tauc plot of $Cs_2Ag(Sb_xBi_{1-x})Br_6$ thin films on glass based on the absorption coefficient measured by UV-visible spectrophotometry. (b) Tauc plot from PDS measurements of $Cs_2Ag(Sb_xBi_{1-x})Br_6$ thin films on quartz. (c) Bandgaps extract from the Tauc plots in a and b. Only fitting of $Cs_2AgBiBr_6$ is given as examples in (a) and (b). The thickness of the $Cs_2Ag(Sb_xBi_{1-x})Br_6$ films were approximately 200 nm in all cases.

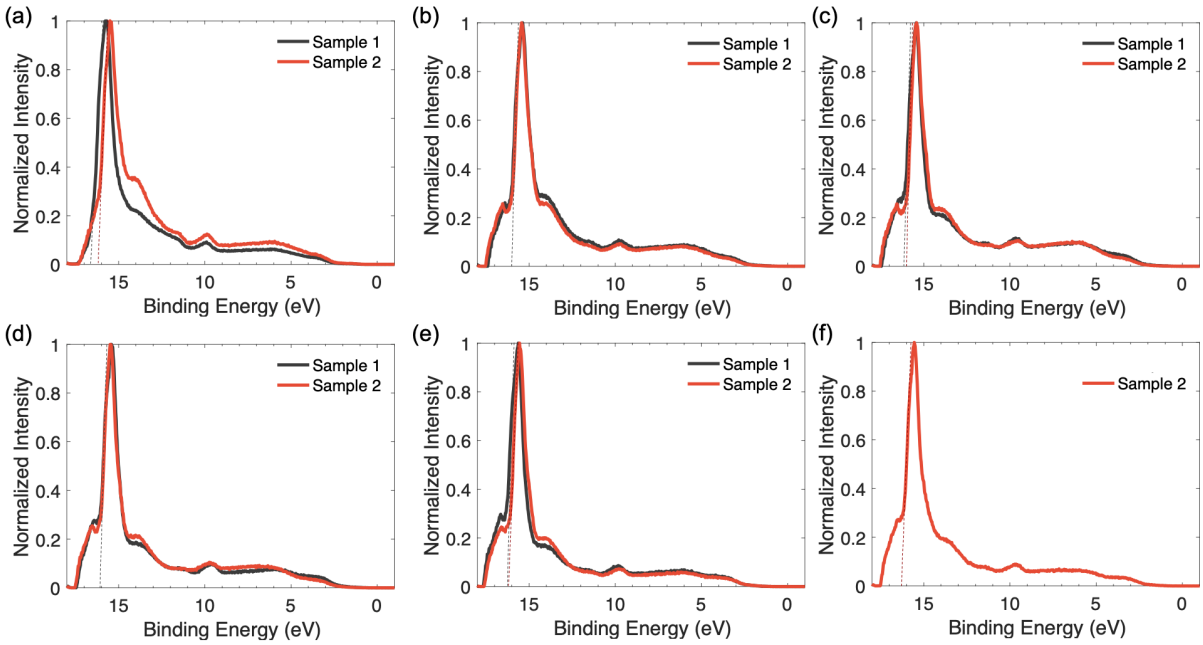

Figure S5. Ultraviolet photoemission spectroscopy measurements of (a) $Cs_2AgSbBr_6$, (b) $Cs_2AgSb_{0.9}Bi_{0.1}Br_6$, (c) $Cs_2AgSb_{0.7}Bi_{0.3}Br_6$, (d) $Cs_2AgSb_{0.5}Bi_{0.5}Br_6$, (e) $Cs_2AgSb_{0.2}Bi_{0.8}Br_6$, (f) $Cs_2AgBiBr_6$ thin films deposited on ITO/glass substrates.

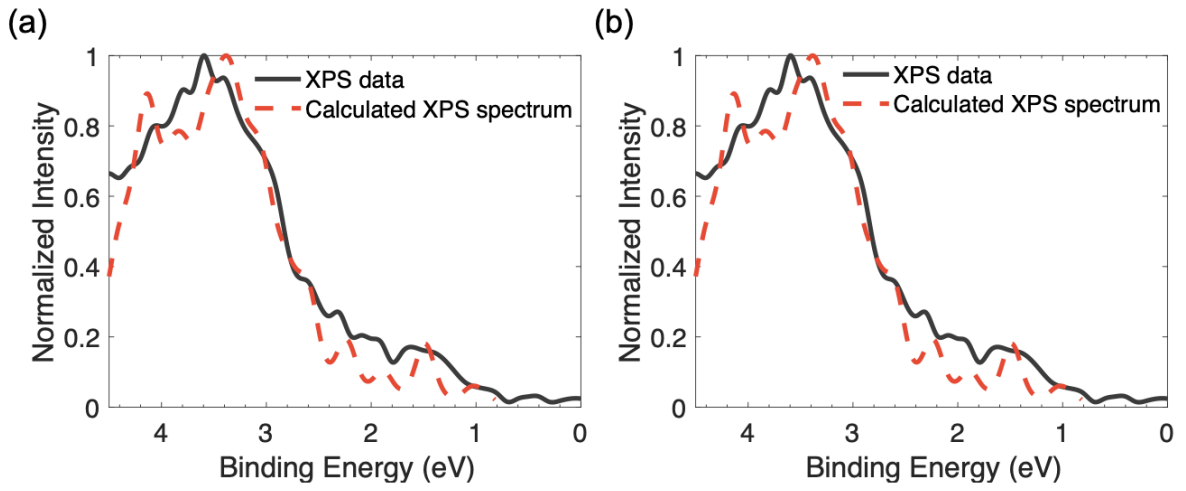

Figure S6. XPS measurements of samples (a) 1 and (b) 2 of $Cs_2AgSbBr_6$ thin film deposited on ITO/glass. The E_F – VB value that gave the best fit of the calculated XPS spectrum to the measured data was 0.81 eV. The calculated XPS spectrum was for $Cs_2AgSbBr_6$.

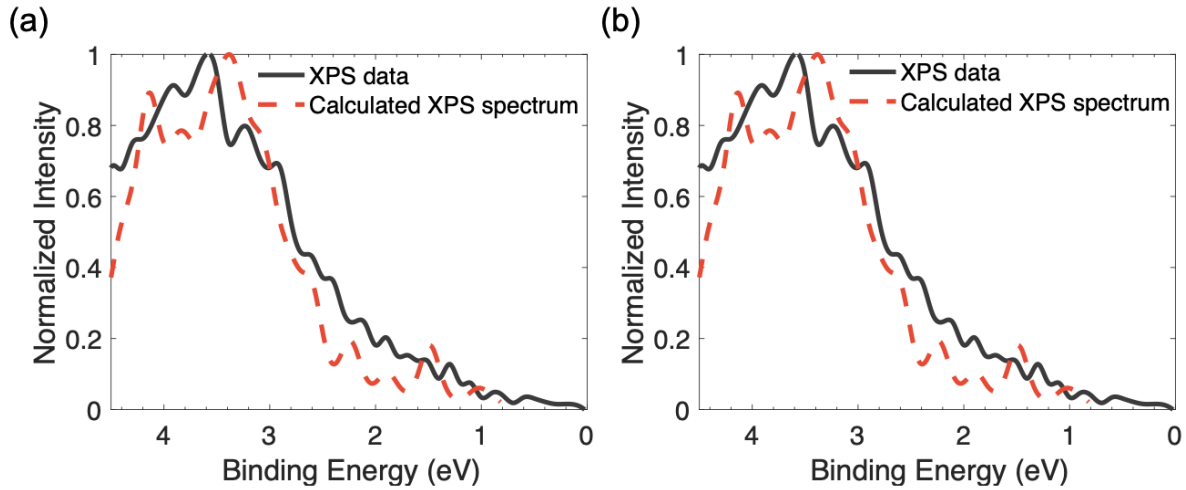

Figure S7. XPS measurements of samples (a) 1 and (b) 2 of $Cs_2AgSb_{0.9}Bi_{0.1}Br_6$ thin film deposited on ITO/glass. The E_F – VB value that gave the best fit of the calculated XPS spectrum to the measured data was 0.81 eV. The calculated XPS spectrum was for $Cs_2AgSbBr_6$.

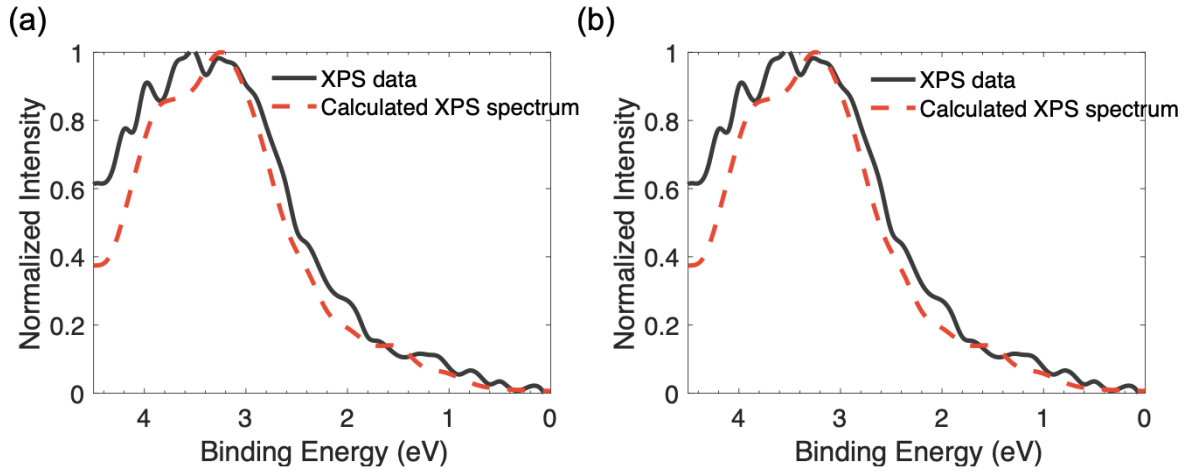

Figure S8. XPS measurements of samples (a) 1 and (b) 2 of $Cs_2AgSb_{0.7}Bi_{0.3}Br_6$ thin film deposited on ITO/glass. The E_F – VB value that gave the best fit of the calculated XPS spectrum to the measured data was 0.82 eV. The calculated XPS spectrum was for $Cs_2AgSb_{0.75}Bi_{0.25}Br_6$.

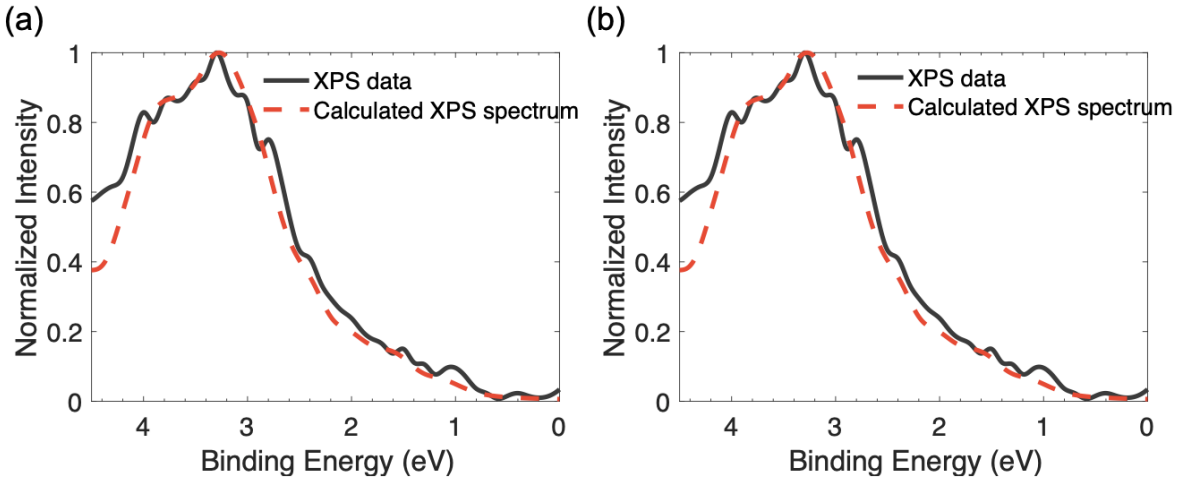

Figure S9. XPS measurements of samples (a) 1 and (b) 2 of $Cs_2AgSb_{0.50}Bi_{0.50}Br_6$ thin film deposited on ITO/glass. The E_F – VB value that gave the best fit of the calculated XPS spectrum to the measured data was 0.81 eV. The calculated XPS spectrum was for the $Cs_2AgSb_{0.50}Bi_{0.50}Br_6$ supercell with the diagonally-similar arrangement of octahedra (Figure S13c).

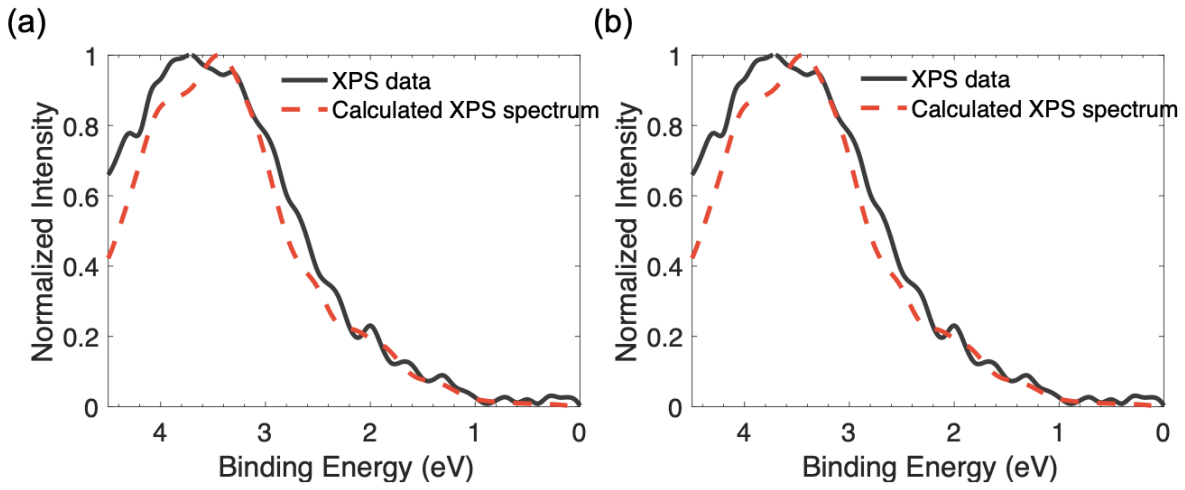

Figure S10. XPS measurements of samples (a) 1 and (b) 2 of $Cs_2AgSb_{0.2}Bi_{0.8}Br_6$ thin film deposited on ITO/glass. The E_F – VB value that gave the best fit of the calculated XPS spectrum to the measured data was 1.11 eV. The calculated XPS spectrum was for $Cs_2AgSb_{0.12}Bi_{0.88}Br_6$.

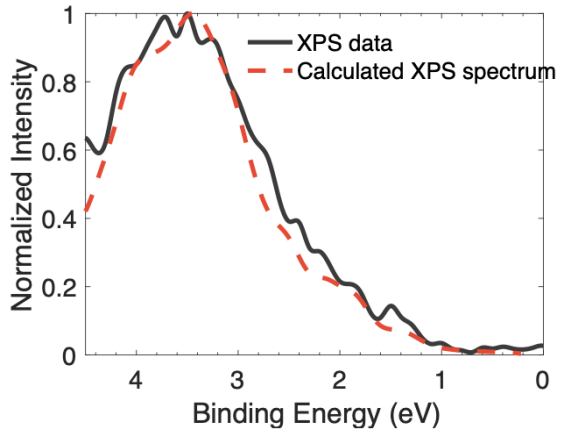

Figure S11. XPS measurements of $Cs_2AgBiBr_6$ thin film deposited on ITO/glass. The E_F – VB value that gave the best fit of the calculated XPS spectrum to the measured data was 1.21 eV. The calculated XPS spectrum was for $Cs_2AgBiBr_6$.

Table S1. Band positions of the $Cs_2Ag(Sb_xBi_{1-x})Br_6$ films determined from the photoemission spectroscopy and photothermal deflection spectroscopy measurements

Nominal Sb/(Sb+Bi) in precursor solution	Workfunction (eV)	E_F – VB (eV)	Bandgap (eV)	Ionization potential (eV)	Electron affinity (eV)
100%	4.82	0.81	2.18	5.63	3.45
90%	5.09	0.81	2.08	5.90	3.82
70%	5.05	0.82	2.10	5.87	3.77
50%	5.04	0.81	2.10	5.85	3.75
20%	4.89	1.11	2.20	6.00	3.80
0%	4.90	1.21	2.25	6.11	3.86

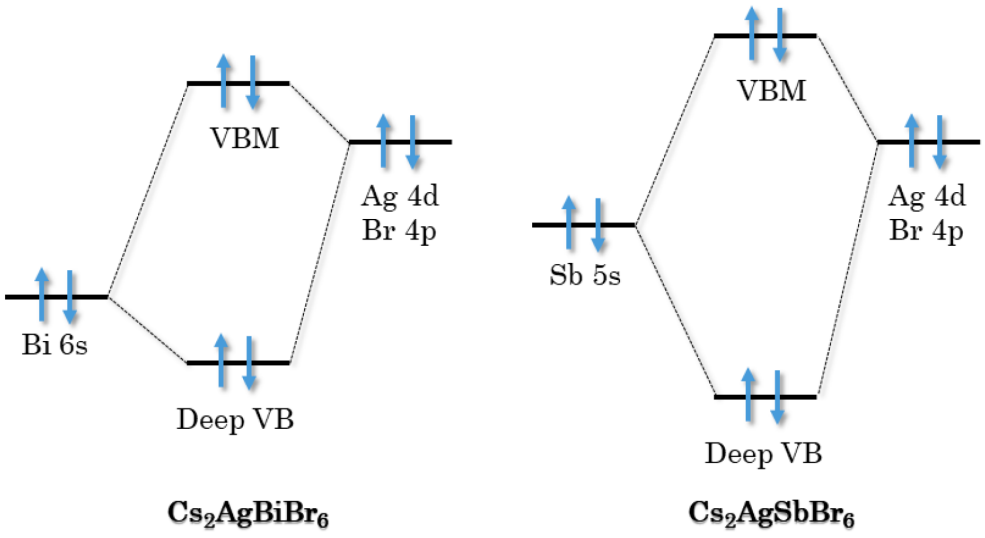

Figure S12. Schematic molecular orbital diagram demonstrating the effect of cationic lone-pair interactions on the VBM position.

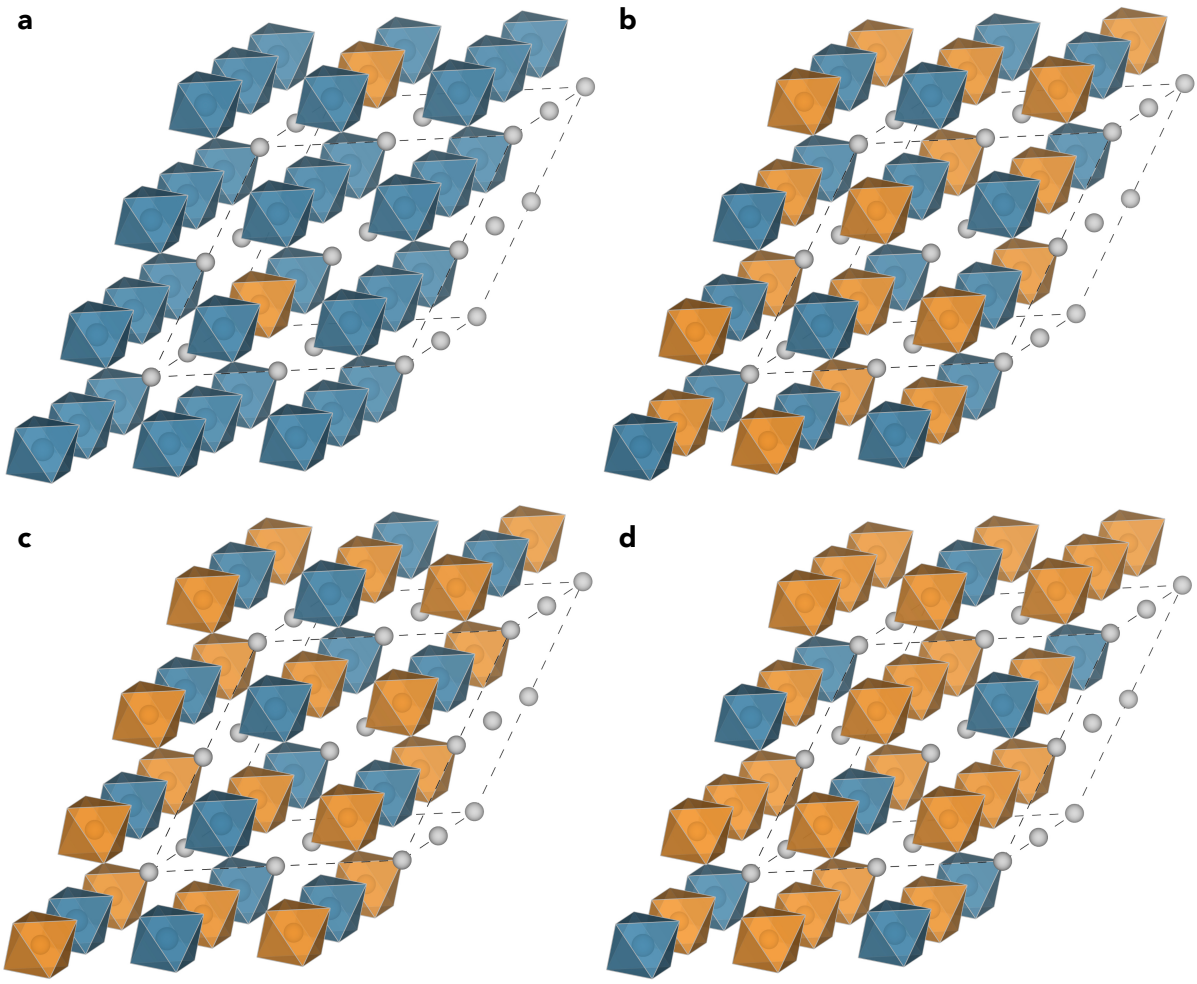

Figure S13. Structures used for the investigation of alloy electronic properties, corresponding to (a) $Cs_2AgSb_{0.125}Bi_{0.875}Br_6$, (b,c) $Cs_2AgSb_{0.5}Bi_{0.5}Br_6$ (in two possible arrangements) and (d) $Cs_2AgSb_{0.75}Bi_{0.25}Br_6$. Sb-based octahedra are coloured orange, Bi-based octahedra are coloured blue, and Ag atoms in silver. Br anions located at octahedral corners, and Cs cations omitted for clarity.

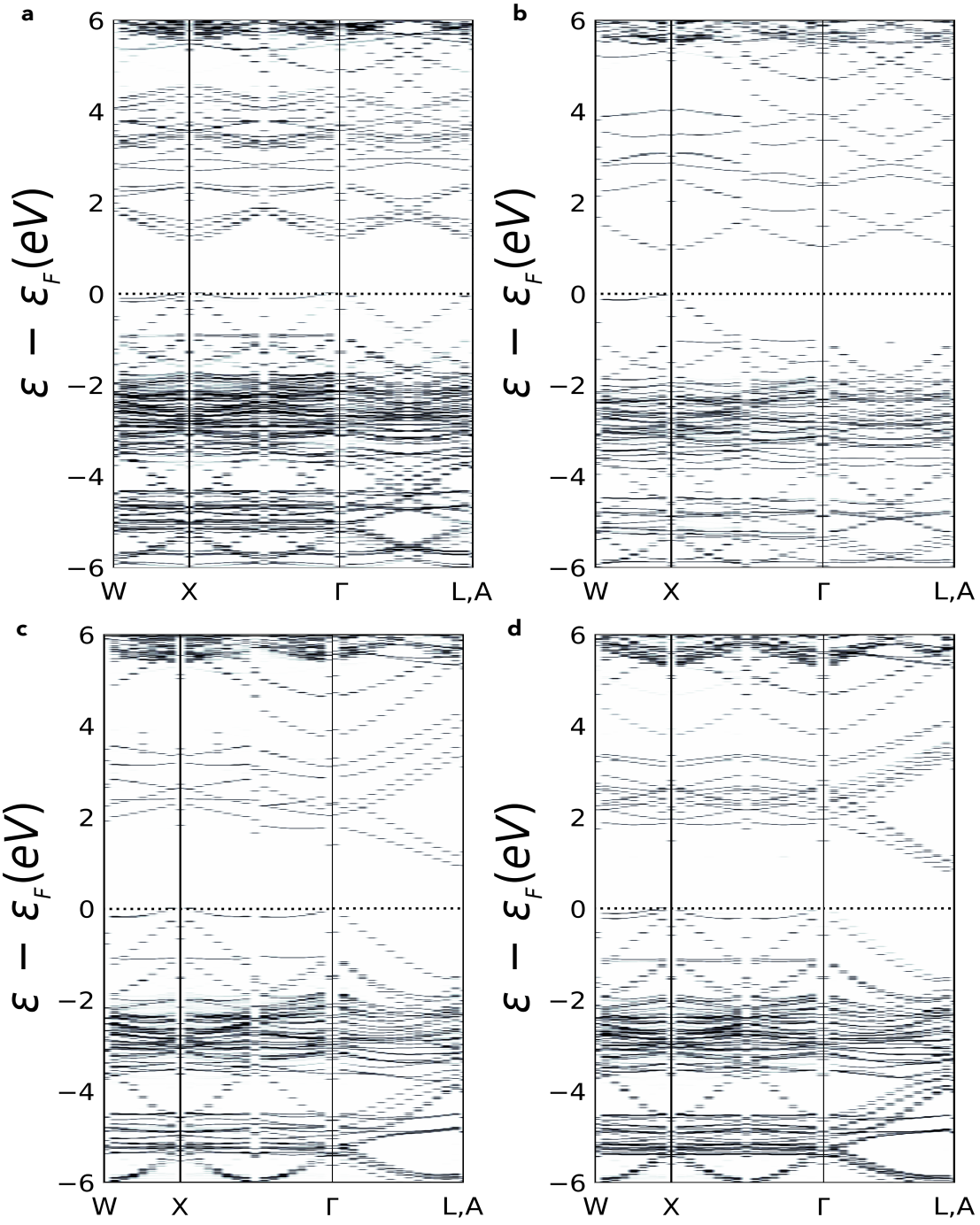

Figure S14. Symmetry-weighted unfolded bandstructures of the simulated alloy materials, for (a) $Cs_2AgSb_{0.125}Bi_{0.875}Br_6$, (b,c) $Cs_2AgSb_{0.5}Bi_{0.5}Br_6$ (in the two arrangements shown in Figure S13) and (d) $Cs_2AgSb_{0.75}Bi_{0.25}Br_6$. Fermi level set to match the VBM in each case. Slight discontinuities in the unfolded bandstructures are due to broken symmetry relations (between the alloy supercells and the original $Fm\bar{3}m$ space group primitive cell) – leading to band splitting and inequivalent directions in reciprocal space, and reduced **k**-point sampling density – due to computational limitations. Corresponding electronic density of states and bandgaps provided in Figure S15 and Table S3 below.

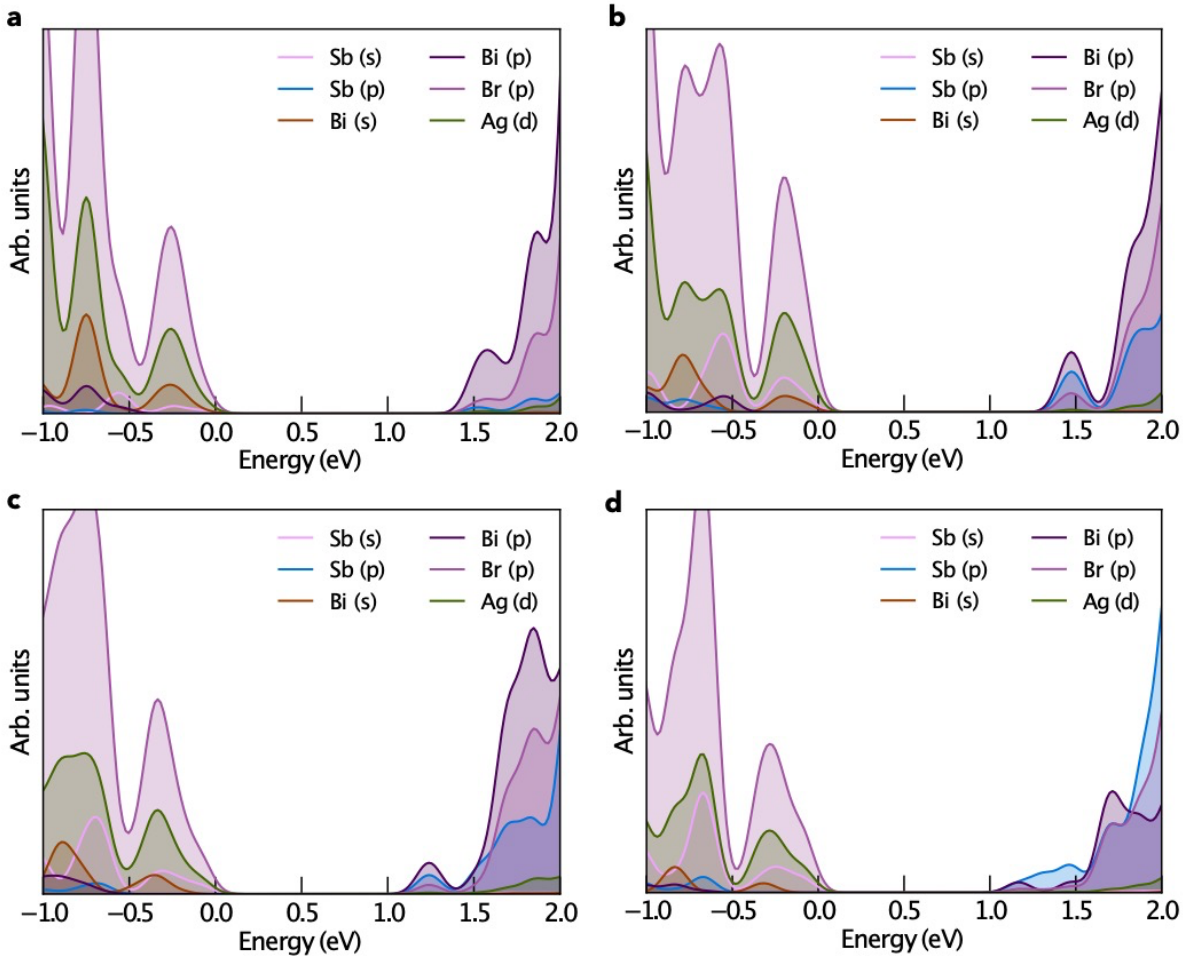

Figure S15. Orbital-projected electronic density of states of the simulated alloy materials, for (a) $Cs_2AgSb_{0.125}Bi_{0.875}Br_6$, (b,c) $Cs_2AgSb_{0.5}Bi_{0.5}Br_6$ (in the two arrangements shown in Figure S13) and (d) $Cs_2AgSb_{0.75}Bi_{0.25}Br_6$. VBM set to 0 in each case. In each case, the VBM is composed of Ag *d*, Br *p* and Sb/Bi s orbital character, while the CBM primarily arises from Sb/Bi *p* – Br *p* interactions, in agreement with the prediction that non-linear orbital mixing at the band edges is the source of the experimentally-observed bandgap lowering.

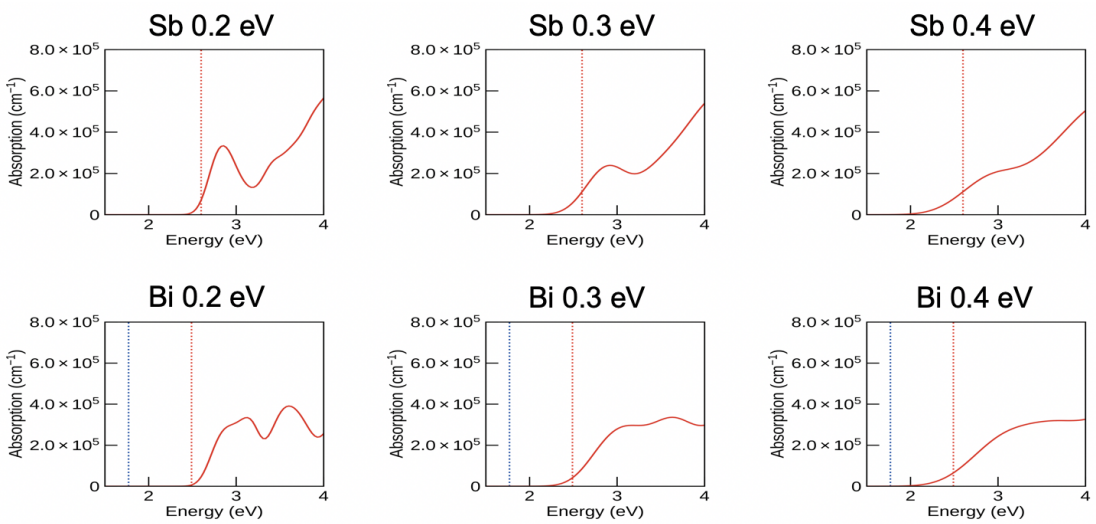

Figure S16. Calculated optical absorption with higher Gaussian broadening (indicated in the energy values in the title), resulting in smeared out peaks. Dashed vertical red line indicates the calculated position of the optical gap.

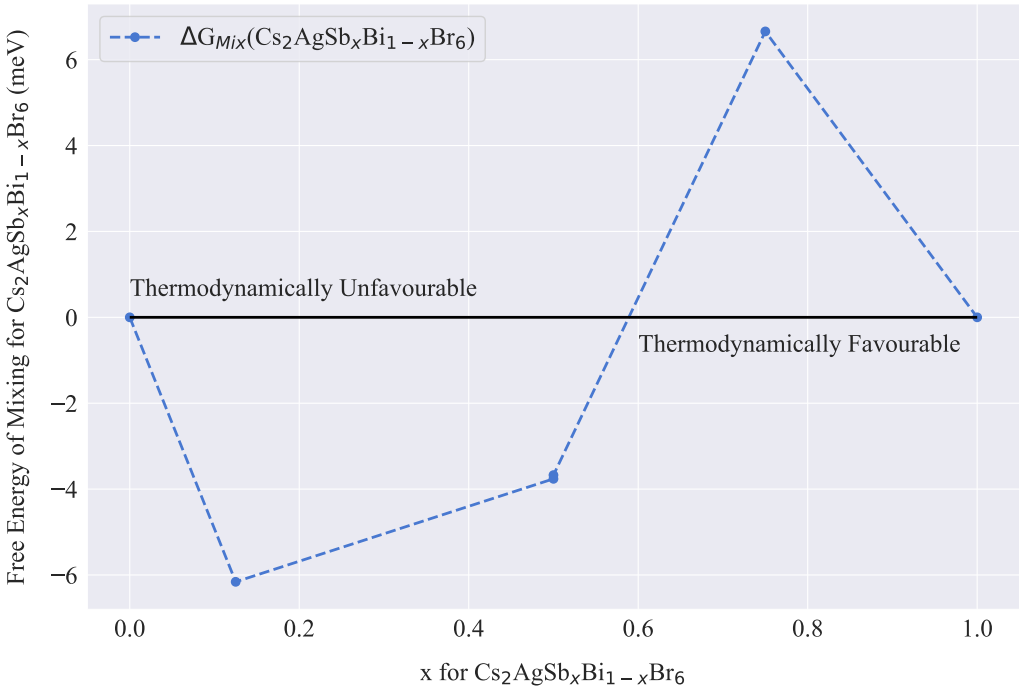

Figure S17. Calculated free energies of mixing for the simulated alloy materials, using equations S4 and S5.

Table S2. Calculated effective mass values for $Cs_2AgSbBr_6$ and $Cs_2AgBiBr_6$ in units of electron mass.

Material	$m_h^{\Gamma\text{-}X}$	$m_h^{X\text{-}W}$	$m_e^{W\text{-}L}$	$m_e^{L\text{-}\Gamma}$
$Cs_2AgSbBr_6$	0.15	0.62	0.26	0.32
$Cs_2AgBiBr_6$	0.18	0.61	0.31	0.45

Table S3. Calculated bandgaps for both the pure and alloy materials, in units of electronvolts.

***x* for $Cs_2AgSb_xBi_{1-x}Br_6$**	0	0.125	0.5 (Figure S13b)	0.5 (Figure S13c)	0.75	1.0
Fundamental Bandgap (eV)	1.77	1.18	0.97	0.94	0.82	1.37

References

1 G. Kresse and J. Hafner, *Phys. Rev. B*, 1993, **47**, 558–561.

2 G. Kresse and J. Hafner, *Phys. Rev. B*, 1994, **49**, 14251–14269.

3 G. Kresse and J. Furthmüller, *Comput. Mater. Sci.*, 1996, **6**, 15–50.

4 G. Kresse and J. Furthmüller, *Phys. Rev. B*, 1996, **54**, 11169–11186.

5 J. P. Perdew, A. Ruzsinszky, G. I. Csonka, O. A. Vydrov, G. E. Scuseria, L. A. Constantin, X. Zhou and K. Burke, *Phys. Rev. Lett.*, 2008, **100**, 136406.

6 A. V. Krukau, O. A. Vydrov, A. F. Izmaylov and G. E. Scuseria, *J. Chem. Phys.*, 2006, **125**, 224106.

7 J. P. Perdew, K. Burke and M. Ernzerhof, *Phys. Rev. Lett.*, 1996, **77**, 3865–3868.

8 P. E. Blöchl, *Phys. Rev. B*, 1994, **50**, 17953–17979.

9 M. Gajdoš, K. Hummer, G. Kresse, J. Furthmüller and F. Bechstedt, *Phys. Rev. B*, 2006, **73**, 045112.

10 L. D. Whalley, *J. Open Source Softw.*, 2018, **3**, 797.

11 A. M Ganose, A. J Jackson and D. O Scanlon, *J. Open Source Softw.*, 2018, **3**, 717.

12 K. T. Butler, C. H. Hendon and A. Walsh, *J. Am. Chem. Soc.*, 2014, **136**, 2703–2706.

13 Y. H. Li, X. G. Gong and S. H. Wei, *Appl. Phys. Lett.*, 2006, **88**, 042104.

14 F. C. Von Der Lage and H. A. Bethe, *Phys. Rev.*, 1947, **71**, 612–622.

15 A. J Jackson, A. M Ganose, A. Regoutz, R. G. Egdell and D. O Scanlon, *J. Open Source Softw.*, 2018, **3**, 773.

16 K. Z. Du, W. Meng, X. Wang, Y. Yan and D. B. Mitzi, *Angew. Chem. Int. Ed.*, 2017, **56**, 8158–8162; *Angew. Chem.,* 2017, **129**, 8270–8274.

17 M. Mayer, *SIMNRA User ' s Guide*, 2017.